Synthesis of NiFeOx nanocatalysts from metal–organic precursors for the oxygen evolution reaction

Quyen Nguyen, Francois Robert, V. Collière, Pierre Lecante, Karine Philippot, Jérôme Esvan, Phong Tran, Catherine Amiens

Synthesis of NiFeOx nanocatalysts from metal-organic precursors for the oxygen evolution reaction

Nguyen Thi Quyen,[1,2,3] Francois Robert, [1,2] Vincent Colliere,[1,2] Pierre Lecante,[4] Karine Philippot,[1,2] Jérome Esvan,[5] Tran Dinh Phong,[3]* Catherine Amiens,[1,2]*

[1] CNRS, LCC (Laboratoire de Chimie de Coordination), 205 Route de Narbonne, BP 44099, F-31077 Toulouse Cedex 4, France.
[2] Université de Toulouse, UPS, INPT, F-31077 Toulouse Cedex 4, France
[3]University of Science and Technology of Hanoi, Vietnam Academy of Science and Technology of Hanoi, 18 Hoang Quoc Viet, Hanoi, Vietnam.
[4]CEMES-CNRS, Université de Toulouse, CNRS, UPS, 29 rue J. Marvig, 31055 Toulouse, France
[5]CIRIMAT, Université de Toulouse, CNRS-INPT-UPS, 4 Allée Emile Monso, BP 44362, 31030 Toulouse, France

Corresponding authors:
Catherine Amiens : catherine.amiens@lcc-toulouse.fr
Tran Dinh Phong: tran-dinh.phong@usth.edu.vn

Abstract

Production of hydrogen from the renewable source that is water requires the development of sustainable catalytic processes. This implies, among others, to develop efficient catalytic materials from abundant and low cost resources and investigate their performance, especially in the oxidation of water as this half reaction is the bottle-neck of the water splitting process. For this purpose, NiFe-based nanoparticles with sizes *ca*. 3-4 nm have been synthesized by an organometallic approach and characterized by complementary techniques (WAXS, TEM, STEM-HAADF, EDX, XPS, ATR-FTIR). They display a Ni core and a mixed Ni-Fe oxide shell. Once deposited onto FTO electrodes, they have been assessed in the electrocatalytic oxygen evolution reaction in alkaline conditions. Three different Ni/Fe ratios (2/1, 1/1 and 1/9) have been studied in comparison with monometallic counterparts. The Ni2Fe1 nanocatalyst displayed the lowest overpotential (320 mV at j = 10 mA/cm^2) as well as an excellent stability over 16 h.

Keywords : bimetallic nanoparticles, electro-catalysis, oxygen evolution reaction, water-splitting.

I. Introduction

Water splitting (WS) is an attractive technology for the large scale production of hydrogen.[1] WS is based on two half reactions: an oxygen evolution reaction (OER) and a hydrogen evolution reaction (HER). OER is considered to be the bottleneck because it is at the same time thermodynamically uphill and sluggish, requiring multistep proton-coupled electron transfers.[2] Therefore, many efforts have been focused on the development of efficient catalysts to accelerate this OER.[3] State-of-the-art water oxidation electrocatalysts (WOC) are oxides of Iridium and Ruthenium due to their excellent activity in both acidic and basic conditions and superior stability.[4, 5] However, they suffer from unsatisfying sustainability (high cost and scarcity) which greatly hinders their commercial application.[6] To promote the production of hydrogen from water splitting at large scale, it is thus mandatory to develop alternative WOCs from non-noble and low-cost metals that also display high efficiency and robustness. For this purpose, metal oxides,[3,7] hydroxides,[8,9] and oxyhydroxides,[10-13] phosphides[14] of earth-abundant transition metals like Mn, Fe, Co, Ni, Cu are the most promising candidates. Mixed metal oxides (or bimetal oxides) have received great attention as they usually exhibit both superior catalytic performances and stability than their parent metal oxides.[15] Thus, Ni-Fe oxide-based catalysts are significantly more active for the OER in alkaline conditions than their Ni and Fe counterparts. This higher activity is attributed to (i) a change in the electronic structure of the catalyst, (ii) an improved conductivity, and (iii) an increased number of redox active centers.[16] Ni-Fe oxide-based catalysts consisting of 60-90 wt% of Ni have been shown to display the best OER activity.[17]

Since the electrocatalytic activity of a material strongly depends on its electrochemically active surface area, one strategy to boost the performance is to decrease its size in order to have a higher density of surface sites per mass unit, like e.g. using nanoparticles (NPs).[18] To the best of our knowledge most of the publications on Ni-Fe based OER catalysts investigate the activity of thin-films and only a few are devoted to the use of Ni-Fe NPs.[19-22] Note that addition of a stabilizer (like ligands) is usually required to control the growth of NPs (in terms of size, morphology, surface state, dispersability, *etc*.). In this respect, the organometallic synthesis method can provide appropriate answers as it allows to obtain metallic NPs with

good control in size and surface state in mild conditions, that already proved to be efficient nanocatalysts [23, 24] including for water splitting.[25-28]

We thus describe here a new approach to access Ni-Fe based nanocatalysts and discuss on their OER activity in alkaline conditions as a function of their Ni/Fe ratio (2/1, 1/1 and 1/9) in comparison with Ni and Fe counterparts as reference samples. First, Ni-Fe core-shell NPs were synthesized by the organometallic method in usual conditions (organic solvent, inert atmosphere) to control their size, morphology and structure. Then, these NPs were exposed to air and transferred into water *via* a ligand exchange process with the amino phosphonic acid (APA) ligand. The activity of the final nanocatalysts in OER was studied in KOH 1 M, together with their stability.

II. Results and Discussion

1. Synthesis and characterization of the nanocatalysts

NiFe NPs of composition 1Ni/1Fe were synthesized from an equimolar mixture of bis-1,5-cyclooctadiene nickel complex, $Ni(COD)_2$, and bis(bis(trimethylsilyl)) iron (II) complex, $[Fe(N(SiMe_3)_2)_2]_2$ in anisole, as reported by O. Margeat *et al*.[29] Hydrogen was used as the reducing agent and hexadecylamine (HDA) was added as stabilizer to control the growth of the NiFe NPs (**Scheme 1**, first step). Hexamethyldisilazane (HMDS), the amine resulting from the reduction of $[Fe(N(SiMe_3)_2)_2]_2$ may also contribute to the NP stabilization. By adjusting the initial $Ni(COD)_2$/$[Fe(N(SiMe_3)_2)_2]_2$ molar ratio to 2/0.5, the same protocol led to NPs of composition 2Ni/1Fe. These as-synthesized NPs were then exposed to air for 4 days to form a metal oxide layer on their surface (**Scheme 1**, second step). Hereafter, these two samples will be referred to as NiFeOx-1/1 (for composition 1Ni/1Fe) and NiFeOx-2/1 (for composition 2Ni/1Fe). The oxide layer plays a major role not only in protecting the residual Ni core but also in the grafting of the amino phosphonic acid (APA) ligand during the ligand exchange process (**Scheme 1**, third step), which is a key step to obtain NPs that can be dispersed in water (*see below*).

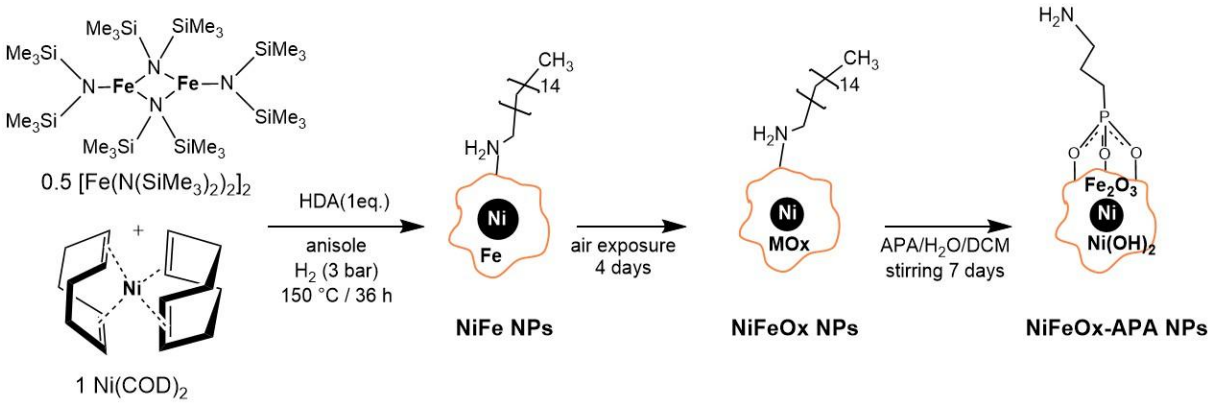

***Scheme 1**. Synthesis of APA-functionalized NiFeOx NPs with composition 1Ni/1Fe (M in MOx = Ni or Fe; DCM = dichloromethane).*

a) **b)**

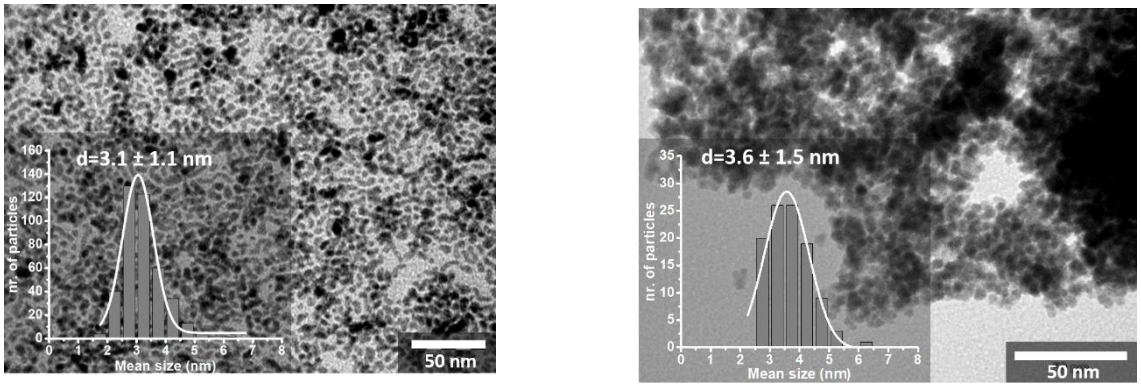

Figure 1. *TEM images and corresponding size histograms of a) NiFeOx-1/1 and b) NiFeOx-2/1. (scale bars = 50 nm)*

Figure 1 shows transmission electron microscopy (TEM) images of the NPs after their oxidation in air (step 2). They display an average diameter of 3.1 ± 1.1 nm (**Figure 1a**) and 3.6 ± 1.5 nm (**Figure 1b**) for NiFeOx-1/1 and NiFeOx-2/1, respectively. The atomic distribution of Ni and Fe within these oxide NPs was studied by atom resolved microscopy (ARM). This technique allowed us to confirm the bimetallic character of the NPs. However, the results concerning the distribution of the two elements inside the NPs were not conclusive, mostly due to the small size of the NPs, similarly Z-contrasting metals, and lack of statistics (See SI, **Figures S1, S2**).

Regarding the structure, the Wide Angle X-Ray Scattering (WAXS) diagrams of NiFeOx-1/1 and NiFeOx-2/1 (**Figure 2)** both show peaks at 20.1, 23.2, 33.1, and 39.1° being characteristic of fcc Ni, and peaks at 16.1 and 27.8° which fit well with the patterns of maghemite or magnetite. Note that these two oxide phases cannot be distinguished with this experimental set-up. The presence of crystalline NiO cannot be confirmed or disproven as the

experimental peaks are quite large, due to the small size of the cristalline domains, and its typical diffraction peaks should be close to those of Fe_2O_3 and/or Ni. Oxidation in air thus leads to full oxidation of Fe but only partial oxidation of Ni as a fcc Ni contribution (superior for the 2Ni/1Fe composition) is still observed, which suggests the formation of a passivating oxide layer. These observations also suggest that at this stage most of the NPs comprise a Ni rich core surrounded by an oxide layer comprising probably Fe and Ni, as drawn in **Scheme 1**.

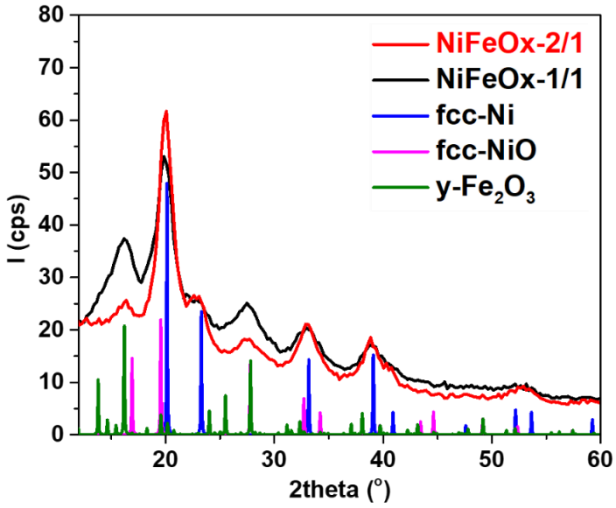

***Figure 2**. WAXS diagrams of NiFeOx-2/1 (red trace) and NiFeOx-1/1 (black trace) with reference diagrams of fcc-Ni (blue trace, PDF 04-010-6148), fcc-NiO (pink trace, PDF 00-044-1159), and γ-Fe_2O_3 (green trace, PDF-01-089-5894).*

ICP-OES analysis revealed metal contents (wt%) no larger than 49% and 31% for NiFeOx-1/1 and NiFeOx-2/1, respectively, thus indicating a large amount of organic ligands that were identified by Fourier Transform Infra-Red (FT-IR) spectroscopy (**Figure S3**) as HDA.

In order to facilitate their dispersion in the hydroalcoholic Nafion solution used to prepare the catalyst inks (*see below*), the NP surface was modified by exchanging HDA for 3-aminopropyl phosphonic acid (APA). This was done by adapting a previously reported ligand exchange process.[30] In brief, a basic solution of APA in water (pH = 8) was added to a solution of the NiFeOx NPs in dichloromethane and the biphasic system was mechanically stirred for 7 days. The change in color of the aqueous phase from colorless to black was a first indication of the successful grafting of the hydrophilic APA at the surface of the NPs

(**Figure S4**). Then the NPs were magnetically separated and washed intensively with water, ethanol, and diethyl ether to eliminate the free ligands, and finally dried in air. The APA-functionalized NPs will be hereafter referred to as NiFeOx-1/1-APA and NiFeOx-2/1-APA.

The now much higher metal content (> 85% in each case) and flatness of the FT-IR spectra of these samples in the 2000-4000 cm^{-1} range (**Figure 3**, c-black and d-pink traces) indicate the efficient release of HDA. Furthermore, the single broad band observed at *ca.* 990 cm^{-1} agrees well with the expectation for Fe-O-P vibrations.[30-32] This indicates that APA has been successfully grafted on the surface of the NiFeOx NPs through a covalent Fe-O-P bonding. The absence of P=O or P-OH vibrations also suggests that APA is likely grafted in a symmetrically tridentate binding mode rather than in a bidentate or monodentate one (**Scheme 1**).[33, 34] XPS analysis further confirmed the anchoring of APA on NiFeOx NPs as both NiFeOx-1/1-APA and NiFeOx-2/1-APA show a P $2p_{3/2}$ peak at 133.6 eV (**Figure 4a**) which is in good agreement with that reported for phosphated magnetite NPs.[35]

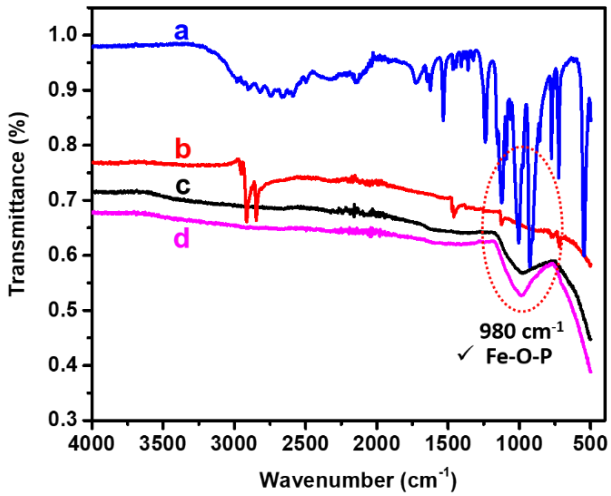

***Figure 3**. FT-IR spectra of a) APA (blue trace), b) NiFeOx-2/1 (red trace), c) NiFeOx-2/1-APA (black trace), and d) NiFeOx-1/1-APA (pink trace)*

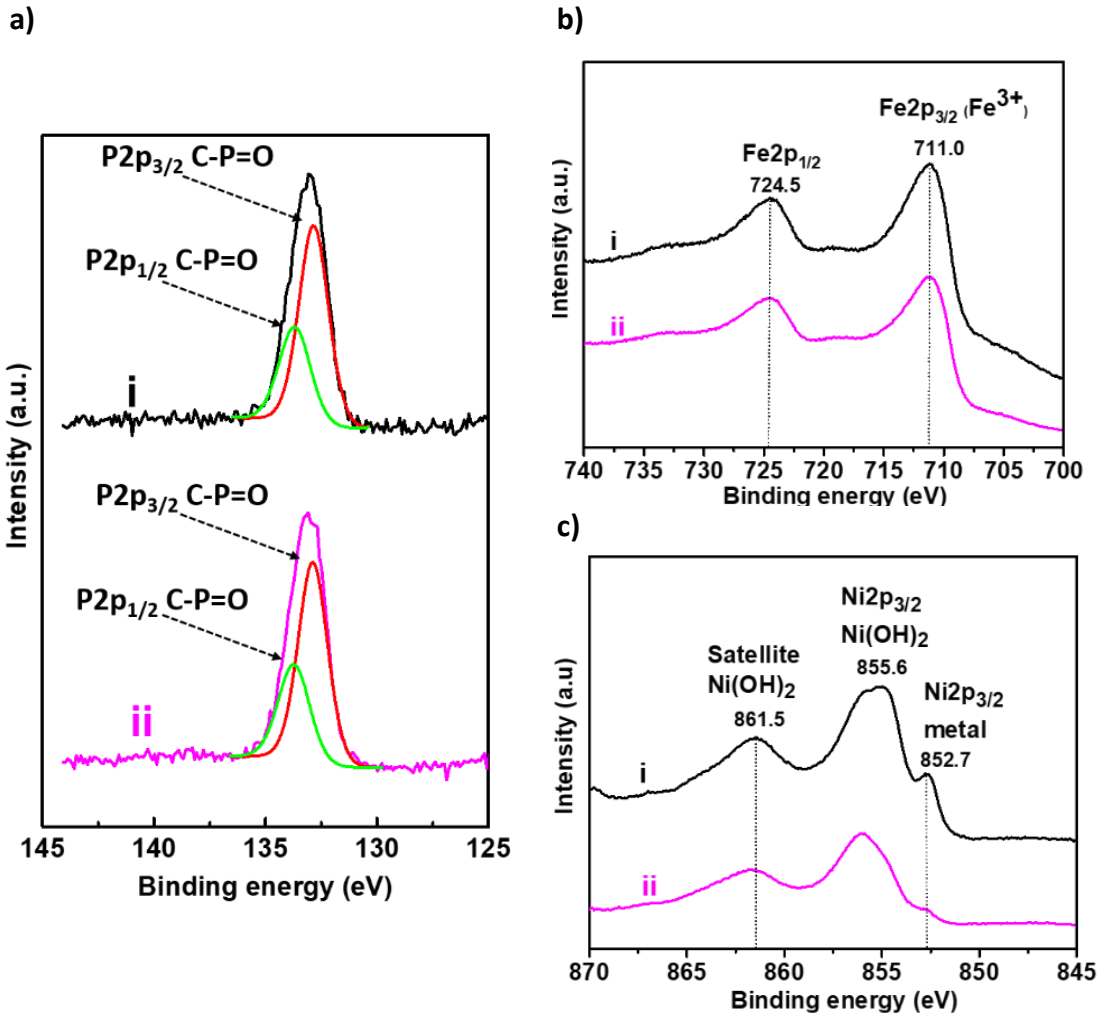

***Figure 4**. XPS spectra of NiFeOx-2/1 -APA (i, top, black trace) and NiFeOx-1/1 -APA (ii, bottom, pink trace): a) P 2p region, b) Fe 2p region (Fe^{3+} satellite peak at 718 eV) and c) Ni 2p region.*

XPS also provided the chemical valence state of Ni and Fe in the different samples. The Fe $2p_{3/2}$ and Fe $2p_{1/2}$ peaks are found at 711.0 eV and 724.4 eV, respectively, which are characteristic values for the Fe^{3+} species (**Figure 4b**). These binding energies are in good accordance with those reported for Fe_2O_3.[36, 37] Concerning Ni $2p_{3/2}$ spectra, the intense peak observed at 855.6 eV as well as the satellite peak at 861.5 eV indicate the presence of $Ni(OH)_2$ species in both NiFeOx-1/1-APA and NiFeOx-2/1-APA (**Figure 4c**). Interestingly, the peak at 852.7 eV could be assigned to the Ni $2p_{3/2}$ peak of Ni metal, indicating the persistence of a Ni core in the NPs even after their transfer into the aqueous phase. From the spectra recorded, the presence of Ni oxide in NiFeOx-1/1-APA and NiFeOx-2/1-APA could not be confirmed nor disproven as there is an overlap between the satellite peak for Ni metal and the main peak for $Ni(OH)_2$ in the region expected for the Ni2p peak of NiO.

Putting together the available data, the NiFeOx-2/1-APA and NiFeOx-1/1-APA NPs are best described by a Ni core surrounded by a mixed $Ni(OH)_2/Fe_2O_3$ surface layer, in which the Ni/Fe ratio varies depending on the composition of the initial NiFe NPs, and bearing APA ligands at the surface (see **Scheme 1)**.

For comparison purpose in electrocatalysis, NiOx and FeOx NPs were also prepared as monometallic references (hereafter referred to as NiOx-PVP and FeOx-HMDS, respectively; PVP and HMDS stand for polyvinylpyrrolidone and hexamethyldisilazane, the polymer and ligand used to stabilize the NiOx and FeOx NPs, respectively), as well as a Fe-rich bimetal oxide nanocatalyst of composition 1Ni/9Fe (hereafter referred to as NiFeOx-1/9-HMDS) to enlarge the range of compositions assayed. Note that no HDA was added during the synthesis of the 1Ni/9Fe NPs. Details on their synthesis and characterization are reported in the ESI - Section 2 and 3. It is noteworthy that 1) the average sizes of the NPs in these nanocatalysts (**Figures S5-6** and **11,** and **Table 1**) are comparable to those of NiFeOx-2/1-APA and NiFeOx-1/1-APA given the width of the size distributions and error bars, 2) oxidation states of Ni and Fe in these reference nanocatalysts are identical to those in NiFeOx-2/1-APA and NiFeOx-1/1-APA (**Figures S8, 10 and 13**), and 3) satisfactory dispersion in aqueous phase is achieved for all samples even though their surface coatings are different (APA, PVP or HMDS). Indeed, thanks to the PVP coating, NiOx-PVP was easily dispersed in water. Satisfactory dispersion in water was also achieved with the HMDS-coated nanocatalysts, FeOx-HMDS and NiFeOx-1/9-HMDS, most likely due to the formation of multilayers of HMDS ligands ultimately exposing the amine groups to water and facilitating hydrogen bonding (and due to the absence of HDA).[38]

2. Investigation of the catalytic activity in OER

This investigation was carried out in alkaline conditions (1 M KOH). To do so, a catalyst ink was prepared using a Nafion solution and then drop-casted onto a FTO electrode at the loading mass density of 2.6×10^{-4} g/cm^2 for each nanocatalyst (*see details in the experimental section*).

2.1. Cyclic voltammetry studies

We first investigated the electrochemical properties of all nanomaterials by cyclic voltammetry (**Figure 5**). The NiOx-PVP reference showed a quasi-reversible wave at $E_{1/2}$ of 1.43 V *vs.* RHE which is assignable to the Ni^{3+}/Ni^{2+} couple, prior to the emergence of the O_2-evolution catalytic wave at the onset potential of 1.53 V *vs.* RHE (**Figure 5b**, black trace). Actually, similar features have been reported for Ni-based O_2-evolution catalysts in alkaline conditions where the pre-catalytic wave was attributed to the oxidation of $Ni(OH)_2$ to NiOOH (*eq.1*).[39-42]

$$Ni(OH)_2 + OH^- \rightarrow NiOOH + H_2O + e^- \quad \text{(eq. 1)}$$

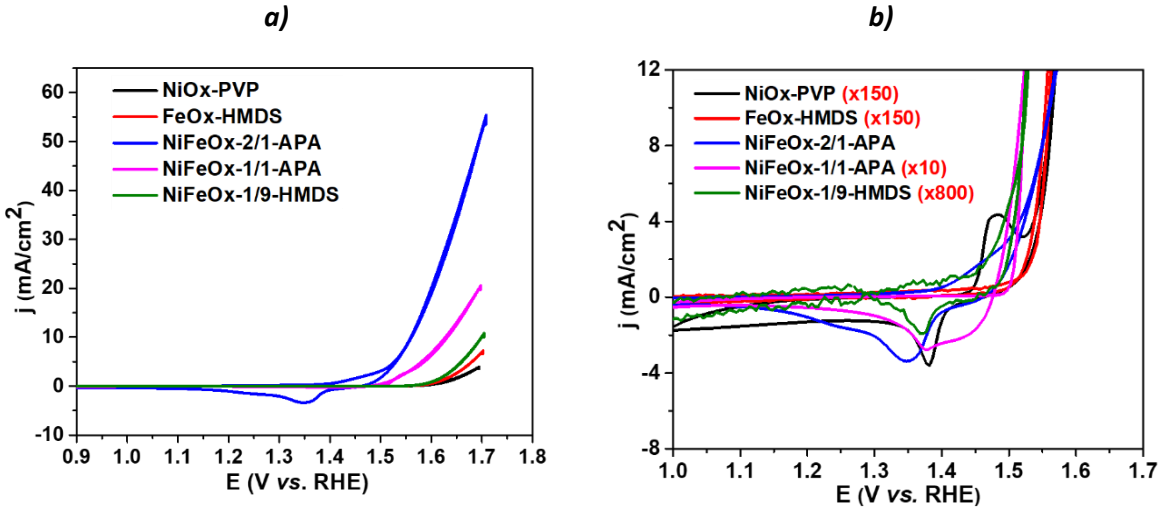

Figure 5. *a) Cyclic voltammograms (CVs) for NiOx-PVP (black trace), FeOx-HMDS (red trace), NiFeOx-2/1-APA (blue trace), NiFeOx-1/1-APA (pink trace), and NiFeOx-1/9-HMDS (green trace) in 1 M KOH. b) Zoom in the region where redox events occur.*

The FeOx-HMDS reference showed a O_2-evolution catalytic event at the onset potential of 1.55 V *vs.* RHE, being rather close to that of NiOx-PVP. However, no obvious redox event was observed prior to the catalytic wave (**Figure 5**, red trace). Regarding the NiFeOx-APA nanocatalysts, depending on the Ni/Fe ratio, a pre-catalytic redox event was observed. NiFeOx-2/1-APA, being the Ni-richest nanocatalyst, showed a small oxidation shoulder at 1.45 V and a reduction peak at 1.35 V *vs.* RHE (**Figure 5**, blue trace). Decreasing the relative content of Ni, *e.g.* in NiFeOx-1/1-APA (**Figure 5**, pink trace) and NiFeOx-1/9-HMDS (**Figure 5**, green trace), caused the progressive decay of these pre-catalytic events. We attribute them to the oxidation/reduction of $Ni(OH)_2$ or NiO species present in the NiFe oxide/hydroxide shell of the nanocatalysts. Regarding the catalytic wave, it emerged at an onset potential of

~1.5 V *vs.* RHE for NiFeOx-2/1-APA and NiFeOx-1/1-APA. It represents a 30-80 mV decrease of the overpotential required to drive the OER, in comparison with the NiFeOx-1/9-HMDS as well as NiOx-PVP and FeOx-HMDS references. These results suggest that the Ni/Fe ratio as well as the accessibility of the surface (which depends on the organic coating) influence the electrochemical behavior, including the electrocatalytic O_2-evolution activity of these nanomaterials.

2.2 Electrocatalytic activity in OER

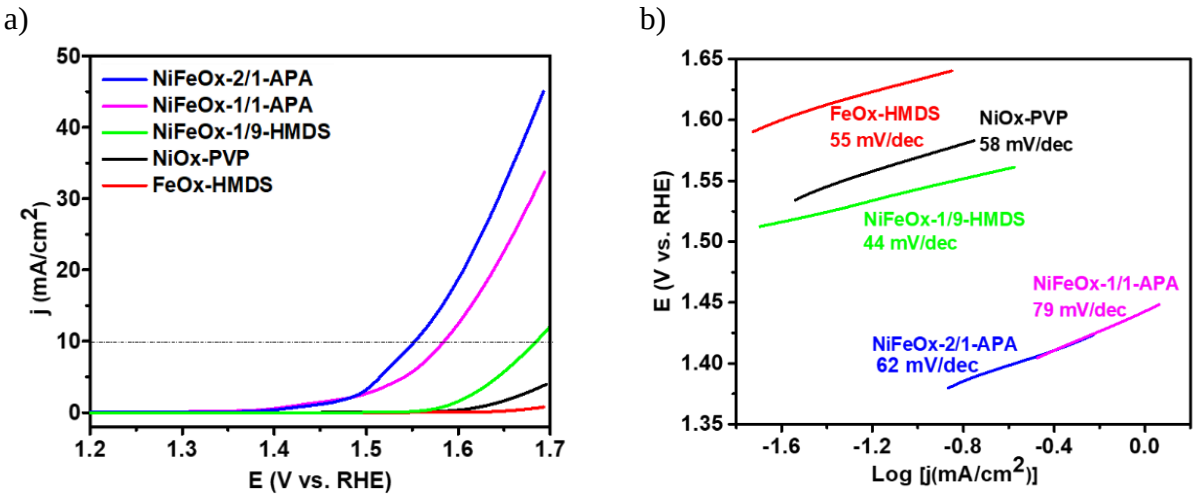

***Figure 6**. a) LSV curves and b) corresponding Tafel plots of NiFeOx-2/1-APA (blue line), NiFeOx-1/1-APA (pink line), NiFeOx-1/9-APA (green line), NiOx-PVP (black line) and FeOx-HMDS (red line) in 1 M KOH , scan rate 5 mV/s.*

Figure 6 shows linear sweep voltammograms (LSV) and corresponding Tafel plots recorded at a scan rate of 5 mV/s for the FTO electrode modified with NiFeOx-2/1-APA, NiFeOx-1/1-APA, NiFeOx-1/9-HMDS, and NiOx-PVP and FeOx-HMDS references. Tafel slops values range from 44 to 79 mV/decade (**Figure 6b**). It suggests that the O_2 evolution involves M-OH/M=O mixed surface species (wherein M is Fe or Ni) and that the water dissociation over these actives sites generating M-O-OH species represents the rate limiting step.[43-45] The variation of Tafel slops values implies a varation of the relative population of M-OH and M=O species on the $NiFeO_x$ catalyst surface when the Ni/Fe ratio changes.[44, 45] We note that NiFeOx-1/9-HMDS showed a higher catalytic current density than FeOx-HMDS at the same applied potential (**Figure 6a**, green and red curves). As these two catalysts have the same surface ligand (HMDS) and comparable sizes (1.6 ± 0.7 and 1.3 ± 0.6 nm for FeOx-HMDS and NiFeOx-

1/9-HMDS, respectively), this indicates a positive influence of the addition of Ni to Fe in NiFeOx NPs, *e.g.* a synergetic effect between Ni and Fe elements, on the catalytic activity. Obviously, such a conclusion would be more definitive if the catalytic activity of NiOx-HMDS NPs could have been recorded. Unfortunately, the synthesis of such a NiOx-HMDS reference failed and we could compare only with NiOx-PVP, which is clearly less active than NiFeOx-1/9-HMDS (**Figure 6a**, black curve).

A closer inspection of the activity of the NiFeOx nanocatalysts shows that it strongly depends on (i) the Ni/Fe molar ratio, and (ii) the organic coating as already suggested by the CV studies. At comparable coating and comparable sizes, NPs with the higher Ni content, *e.g.* NiFeOx-2/1-APA, are more active than those having a lower Ni content, namely NiFeOx-1/1-APA. This result is in line with those published by Ma *et al*.[46] who observed that nanosheets of NiFe layered double hydroxide of 2/1 Ni/Fe composition were more efficient for OER than the 3/1 and 4/1 ones, also in KOH 1 M. Furthermore, the NiFeOx nanocatalysts functionalized by the hydrophilic APA ligand display superior activity than the HMDS coated ones. A rational for this could be that APA insures a better surface accessibility to water molecules than the hydrophobic barrier formed by the multilayers of HMDS, especially as the quantity of organic ligands is higher in this case (**Table S1**), or that the number of surface active sites was increased upon ligand exchange. Unfortunately, identifying the exact contribution of the Ni/Fe molar ratio and of the surface state of the NPs to the catalytic enhancement was not possible. Indeed, the synthesis of NiFeOx NPs having identical Ni/Fe molar ratio, *e.g.* NiFeOx-2/1 NPs, but stabilized by HMDS only, or NiFeOx-1/9 NPs but this time stabilized by APA for comparison purpose, was unsuccessful.

Among all nanocatalysts assayed, NiFeOx-2/1-APA displayed the best catalytic activity as it afforded the highest current density at a given overpotential. To reach the benchmarking catalytic current density (j) of 10 mA/cm^2, this catalyst required only 320 mV, which is 40, 130, and 250 mV less than NiFeOx-1/1-APA, NiFeOx-1/9-HMDS, and FeOx-HMDS, respectively (**Table 1**). Concerning NiOx-PVP, a fast detachement from the FTO electrode was observed before the catalytic current density (j) of 10 mA/cm^2 could be reached. This can be attributed to the high solubility of the NPs in water due to the PVP hydrophilic character and/or a lower stability of the NPs since the PVP provides only a steric

stabilization. These results clearly demonstrate the benefit of having two metals within the oxide catalysts as well as the great impact of the Ni/Fe ratio on the catalysis. It could be due to the redistribution of charges around the Ni and/or Fe metal centers when these two elements are combined in different atomic ratio.[47]

***Table 1**. Overpotentials required to sustain a catalytic current density of 10 mA/cm^2, Tafel slope values, position of the redox peaks observed in cyclic voltammetry, and main physical characteristics of all studied nanocatalysts.*

Sample	**NiFeOx-2/1-APA**	**NiFeOx-1/1-APA**	**NiFeOx-1/9-HMDS**	**FeOx-HMDS**	**NiOx-PVP**
Composition	2Ni/1Fe	1Ni/1Fe	1Ni/9Fe	FeOx	NiOx
Size (nm)	3.6 ± 1.5	3.1 ± 1.1	1.3± 0.6	1.6± 0.7	3.9± 1.1
Surface state	APA	APA	HMDS	HMDS	PVP
η_{10} (mA/cm^2)	320	360	450	570	-
Tafel slope (mV/decade)	62	79	44	55	58
Reduction peak (V *vs*.RHE)	+ 1.35 + 1.24	+ 1.38	+ 1.37	-	+ 1.38
Oxidation peak (V *vs*.RHE)	+ 1.45	+ 1.45	-	-	+ 1.48

2.3 Electrocatalytic stability

We then assessed the stability of all nanocatalysts when operated continuously over an extended period of 16 h. To do so, the catalyst electrodes were first polarized by repeating linear potential scans from 1.23 to 1.70 V *vs.* RHE at a rate of 5 mV/s in 1 M KOH electrolyte until steady I-V curves were achieved. Each electrode was then hold at the potential value where a catalytic current density of 10 mA/cm^2 was determined in the steady I-V curves, namely 1.55 V (NiFeOx-2/1-APA NPs), 1.59 V (NiFeOx-1/1-APA NPs), 1.68 V (NiFeOx-1/9-

HMDS NPs), and 1.8 V (FeOx-HMDS NPs) *vs.* RHE (**Figure 7**). The NiOx-PVP reference was the less stable, and by far, as it readily detached from the electrode surface during the O_2 evolution catalysis. Contrarily, FeOx-HMDS showed an initial catalytic current density of ~8.5 mA/cm^2 but then experienced a fast degradation before reaching a stable current density of ~4 mA/cm^2 (**Figure 7a**, red trace). A decrease in catalytic current density was also observed for the NiFeOx-1/1-APA electrode (**Figure 7a**, pink trace), whereas the NiFeOx-2/1-APA electrode showed a rather stable catalytic current density over the 16 h of operating time (**Figure 7a**, blue trace). We also noticed an interesting behavior for the case of the NiFeOx-1/9-HMDS catalyst. Its initial catalytic current density increased gradually from ~8.5 mA/cm^2 to ~13 mA/cm^2 where it reached a plateau after ~3 h of operation (F**igure 7a**, green trace). We attribute this catalytic enhancement to the oxidative removal of HMDS ligands which makes the surface of the NiFeOx-1/9-HMDS catalyst more accessible to water.

From these results, we can conclude that the best NiFeOx-APA nanocatalyst, both in terms of catalytic activity and stability, is that with the Ni/Fe ratio of 2/1, probably due to a particular synergetic effect at this composition and accessible surface active sites, thanks to the exchange of HDA by APA.

LSV measurements recorded for the NiFeOx-2/1-APA sample after the chronoamperometric experiment showed that this sample displayed almost the same activity as before (**Figure 7b**). The only noticeable difference is the presence of a clear pre-oxidation peak after this experiment, attributed to the Ni^{3+}/Ni^{2+} couple *(see above)*.

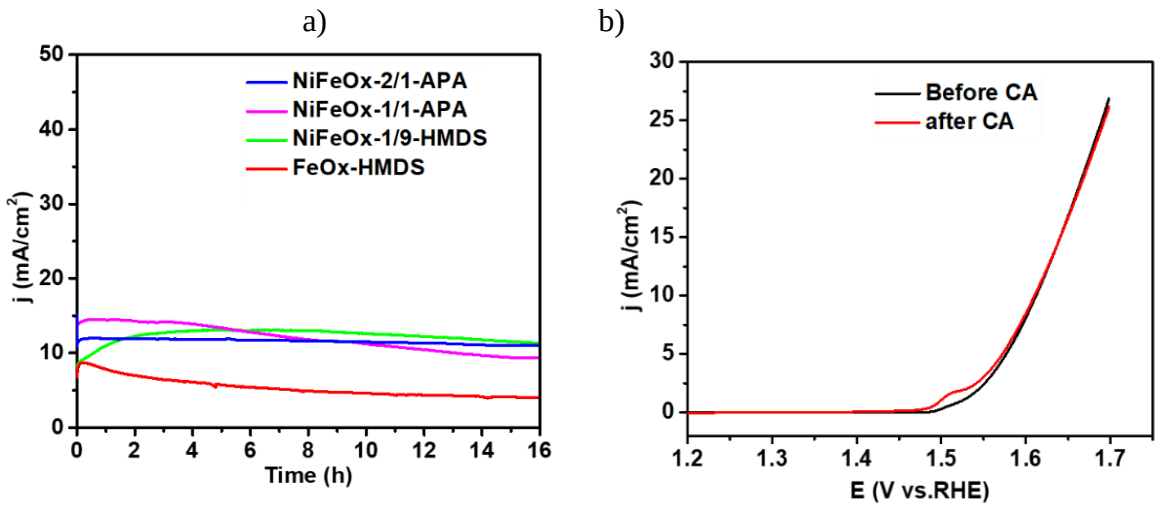

***Figure 7**. a) Chronoamperometry assessment of NiFeOx-2/1-APA (blue line), NiFeOx-1/1-APA (pink line), NiFeOx-1/9-HMDS (green line), and FeOx-HMDS (red line) at a fixed applied potential of respectively 1.55 V, 1.59 V, 1.68 V and 1.8 V vs. RHE in 1 M KOH; b) LSV curves of NiFeOx-2/1-APA before and after the CA test.*

With a stability up to 16 h at j = 10 mA/cm^2, NiFeOx-2/1-APA is much more stable than amorphous NiFe oxide NPs of *similar size* (~ 4 nm) incorporated in carbon black that were stable for only 6 h in identical conditions.[19] The stability of NiFeOx-2/1-APA can also be compared to that of nanocatalysts of larger size (~19.8 nm) but *comparable mixed oxide surface* from Manso *et al.*[20] In this work NPs with a NiOx core and mixed NiFeOx shell showed a stability for 2 h at j = 10 mA/cm^2 in the same conditions. Comparison with literature data thus emphasizes the higher stability of the NiFe nanocatalysts reported herein.

Yet, it is difficult to get a meaningful comparison of the performance of these new NiFeOx nanocatalysts with previous literature data as 1) they are scarce, and 2) even though the total amount of Ni and Fe deposited onto the electrodes can be known from ICP-OES analysis of the catalyst, determining the exact amount of electroactive sites is always challenging and debatable for nanocatalysts, especially for bimetallic systems for which the exact composition of the surface is seldom known. Here, assuming that all Ni and Fe atoms within the NiFeOx NPs contribute to the performance of the nanocatalysts, TOFs values of 0.016 s^{-1} and 0.012 s^{-1} were calculated for the NiFeOx-2/1-APA and NiFeOx-1/1-APA catalysts, respectively, and a value of 0.007 s^{-1} for NiFeOx-1/9 (see ESI-**Table S1** for more details). These values are significantly lower than the one (0.2 s^{-1}) reported for amorphous $NiFeO_x$ NPs having a size of ~ 4 nm, close to that of the nanocatalysts reported herein, but deposited onto a mesoporous carbon support.[19] The difference in the surface state (stabilization by ligands *vs.* carbon material) as well as the use of a conducting mesoporous carbon support could be reasons for such a difference in electrocatalytic performance. Note that these calculated TOF values represent the lower limit of the catalytic rate because the core atoms cannot directly participate in OER as catalysis occurs on the NP surface. Unfortunately, a more accurate calculation of the TOF values is not possible as the currently

available data do not provide a clear image of the distribution of Ni and Fe over the NPs, nor a quantification of the actual active sites.

III. Conclusion

In this work, we reported on the successful synthesis of NiFe oxide NPs of sizes below 4 nm having different Ni/Fe ratios by applying an organometallic synthesis method. The synthesis provided well defined NiFe NPs which were subsequently oxidized into NiFeOx NPs by simple air exposure for their investigation in OER in alkaline conditions. Introduction of only one tenth of Ni led to NPs with improved catalytic activity in comparison to that of single metal oxide NPs (FeOx and NiOx NPs) showing that combining Ni and Fe positively contributes to the catalysis as the result of a synergetic effect between the two elements. A hydrophilic surface coating, hence good wettability and dispersibility in water, was successfully imparted to the NiFeOx NPs of 2/1 and 1/1 composition by replacing the hexadecylamine ligand by the hydrophilic 3-aminopropylphosphonic acid ligand. The resultant NiFeOx-APA NPs showed attractive catalytic activity and stability for OER in alkaline conditions (KOH 1M). It was observed that the activity of NiFeOx NPs strongly depends on their surface coating and on the Ni/Fe molar ratio. As such, NiFeOx NPs having APA ligand on their surface showed superior activity in comparison with those coated by the HMDS ligand, probably due to a better accessibility of the surface active sites. The NiFeOx NPs having higher Ni/Fe molar ratio were more active than their counterparts with lower Ni/Fe ratio. Regarding the catalytic rate, NiFeOx-APA showed lower TOFs than that of previously reported amorphous NiFeOx NPs of similar size but dispersed on a mesoporous carbon support [19]. It likely indicates that having tiny particle size, thus high specific surface area, is important but not enough to reach outstanding catalytic performance. Deposition of these NiFeOx-APA NPs onto high surface conducting support like carbon black, CNTs, or graphene could be a suitable approach to further enhance their activity.

IV. Experimental section

4.1. Materials

$Ni(COD)_2$ (>98 %) was purchased from Strem Chemicals and $[Fe[N(SiMe_3)_2]_2]_2$ (> 99 %)from Nanomeps. Hexadecylamine (HDA) (98%), Nafion (5wt% in a mixture of lower aliphatic alcohols and water), 3-aminopropyl phosphonic acid (APA, 98%), were purchased from Sigma-Aldrich. Anisole (99%, from Alfa Aesar) was degassed by three freeze-pump-thaw cycles then dried over activated molecular sieves (4Å) prior use. CH_2Cl_2, diethyl ether and pentane were collected from a MBraun solvent purification equipment (water content below 5 ppm). MilliQ water (28.2 MΩ) was used for all aqueous preparations. FTO slides were cleaned by sonication for 30 minutes first in acetone (Sigma-Aldrich, ≥ 99.5%) and 30 minutes in EtOH (Sigma-Aldrich, anhydrous, > 99.9 %) then let dry at ambient temperature for 1 h before use.

4.2. Preparation of NPs

4.2.1. Preparation of reference samples

a) Ni and Fe oxide NPs (NiOx-PVP and FeOx-HMDS):

Ni[48] and Fe[49] NPs were synthesized following previous publications from our group (ESI, **scheme S1**). The as-prepared Ni and Fe NPs were then exposed to air in the solid state for 4 days in order to get NiOx-PVP NPs and FeOx-HMDS NPs.

b) Fe rich NPs (NiFeOx-1/9-HMDS):

NiFe-1/9-HMDS NPs were synthesized in the same reaction conditions as the iron NPs described above[49] but introducing the adequate ratio of Ni and Fe precursors, namely 1 $Ni(COD)_2$ (10.3 mg; 0.037 mmol) and 4.5 $[Fe(N(SiMe_3)_2)_2]_2$ (141.5 mg; 0.188 mmol) corresponding to a 1/9 Ni/Fe atomic ratio. The NPs were recovered as a black powder (average mass: 17 mg). They were then exposed to air in the solid state for 4 days in order to get NiFeOx-1/9-HMDS NPs. Fe and Ni contents were 27 wt% and 3 wt% respectively, based on ICP-OES analysis.

4.2.2. NiFeOx NPs with 1Ni/1Fe and 2Ni/1Fe composition.

1Ni/1Fe and 2Ni/1Fe NPs were synthesized by following the procedure described in ref. [29] and adapting the Ni and Fe precursor amounts according to the targeted Ni/Fe ratio.

$[Fe(N(SiMe_3)_2)_2]_2$ (141.7 mg ; 0.188 mmol) , $Ni[(COD)_2]$ (*1Ni/1Fe* : 103.2 mg ; 0.375 mmol or *2Ni/1Fe* : 207 mg ; 0.753 mmol). The NPs were recovered as black powders (Average masses : *1Ni/1Fe* : 60 mg or *2Ni/1Fe* : 83 mg). They were then exposed to air in the solid state for 4 days in order to get the corresponding oxide materials denoted as NiFeOx NPs.

4.2.3. Surface modification of NiFeOx with APA (NiFeOx-2/1-APA, NiFeOx-1/1-APA)

A dispersion of NiFeOx NPs (30 mg) in dichloromethane (15 mL) was added to 10 mL of a 7×10^{-3} M solution of APA (pH ~7-8) in a 30 mL closed glass tube. The reacting medium was mechanically stirred for 7 days. Then the aqueous phase was recovered from which the NPs were collected by magnetic separation. The NPs were washed with MilliQ water (5 x 30 mL), ethanol (1 x 30 mL) and diethyl ether (1 x 30 mL) before drying in air for characterization (Recovered mass: ~15.5 mg). ICP-OES NiFeOx-2/1-APA: Ni = 63 wt%, Fe = 29 wt%. NiFeOx-1/1/-APA : Ni = 44 wt%, Fe = 42 wt%.

4.3. Electrochemical characterization

First catalyst inks were prepared by sonicating 3 mg of each catalyst in 1 mL of a 1/4 (v/v) $EtOH/H_2O$ solvent mixture together with 1 µl Nafion 5% as a linker.

The **NiFeOx-2/1-APA, NiFeOx-1/1-APA, NiFeOx-1/9-HMDS, FeOx-HMDS, and NiOx-PVP** WOCs were prepared by depositing 17 µL of the catalyst ink onto a FTO electrode (S = 0.196 cm^2, loading density of 2.6×10^{-4} g/cm^2) followed by a mild annealing process at 100 °C in an oven for 5 h. before testing their catalytic activity in OER.

The LSV, CV, and CA experiments were performed on a PG300-potentiostat using a 3-electrode configuration where the catalyst modified FTO electrode was the working electrode while a Pt rod and a saturated calomel electrode (SCE) $Hg/Hg_2Cl_2/KCl$ 3M were used as counter electrode and reference electrode, respectively. 1 M KOH was used as the electrolyte solution. Argon gas was bubbled through the electrolyte for 5 min before each experiment in order to remove oxygen from the solution.

LSV was run at a scan rate of 5 mV/s from open circuit voltage to 1.7 V *vs*. RHE. CV was run at a scan rate of 5 mV/s between 1.0 V and 1.7 V *vs.* RHE. The durability of the OER catalysts was tested by chronoamperometry at a current density of j = 10 mA/cm^2 for 16 h.

The potential with reference to SCE was converted into RHE using the following equation:

$E_{RHE} = E_{SCE} + 0.059 \times pH + E^{º}_{SCE}$, assuming pH = 14 as the measurements were performed in 1 M KOH. $E^{º}_{SCE}$ was 0.24 V for the reference electrode. Calculation of the overpotential value was done by subtracting the theoretical potential for the OER 1.23 V from the measured potential *vs*. RHE. To calculate the current density (j, mA/cm^2), the intensity of the current was normalized to the geometric surface area of the FTO electrode (S = 0.196 cm^2).

4.4. Characterization techniques

The nanoparticles were characterized by different techniques: Fourier transform infrared spectroscopy (FT-IR) in ATR mode, Transmission electron microscopy (TEM/HRTEM), Wide angle X-ray scattering (WAXS), X-ray photoelectron spectroscopy (XPS), Inductively coupled plasma- Optical emission spectroscopy (ICP-OES).

TEM and HR-TEM: TEM and HR-TEM analyses were performed at "Centre de Microcaractérisation Raimond Castaing", Toulouse. The shape, size and crystallinity of nanoparticles were examined by low resolution TEM (JEOL, JEM-1011 microscope, operating at 100 kV, point resolution of 0.45 nm) and high resolution in high angle annular dark field – scanning transmission electron microscopy mode (HAADF-STEM) (JEM, ARM200F microscope, operating at 200 kV, point resolution of 0.19 nm). The samples were prepared by drop-casting the colloidal solution of NPs onto carbon coated copper grids (400 hexagonal mesh). Then the grids were dried under vacuum for one night before their introduction into the microscope chamber. Size distributions were obtained via the ImageJ software.

ATR-FTIR: Fourier transform infrared spectra of the NPs were recorded in attenuated total reflectance (ATR) mode inside the glove box on a Brucker Alpha spectrophotometer (spectral resolution 2 cm^{-1}) in the range 4000 - 500 cm^{-1}.

XPS: X-ray Photoelectron Spectroscopy measurements were performed at CIRIMAT, on a ThermoScientific K-Alpha with a monochromatised Al Kalpha (hν = 1486.6 eV) source. The X-ray Spot size was 400 µm. The Pass energy was fixed at 30 eV with a step of 0.1 eV for core levels and 160 eV for surveys (step 1 eV). The spectrometer energy calibration was done

using the Au $4f_{7/2}$ (83.9 ± 0.1 eV) and $Ag3d_{5/2}$ (368.2 ± 0.1 eV) photoelectron lines. XPS spectra were recorded in direct mode N (Ec) and the background signal was removed using the Shirley method. XPS High Resolutions spectra were recorded in order to extract the chemical environments of the studied species.

ICP-OES: Iron, Ni and P contents were determined by ICP-OES analysis on a PerkinElmer, Optima 2100 DV equipment. The samples were digested into a mixture of HCl: HNO_3 (3:1 v/v) and then diluted with MilliQ water.

WAXS: Wide-Angle X-ray Scattering measurements were carried out at CEMES - CNRS in Toulouse. The samples were sealed in 1.0 mm (diameter) Lindemann glass capillaries under Argon atmosphere for the non-oxidized nanomaterials or in air for the oxide nanomaterials. The X-ray scattering intensity measurements were performed using a dedicated two-axis diffractometer using the molybdenum Kα (0.071069 nm) radiation monochromatized by a flat graphite crystal. Radial distribution functions (RDF) were obtained after Fourier transformation of the corrected and reduced data.

V. Conflicts of interest

There are no conflicts of interest to declare.

VI. Acknowledgements

We thank CNRS and Université de Toulouse - Paul-Sabatier for financial support. We thank the “Centre de Microcaractérisation Raimond Castaing” in Toulouse for access to the microscopes. T.D.P. acknowledges the National Foundation for Science and Technology Development (NAFOSTED) for funding support (grant number 103.99-2019.328). N.T.Q acknowledges the French embassy in Hanoi for her PhD scholarship (Bourse d`Excellence 2018-2021). F.R. thanks ANR (ANR-17-CE07-0022-01) and Région Occitanie (ALDOCT000355) for financial support.

VII. Authors contributions

Conceptualization – CA, TDP, KP ; Data curation – PL ; Formal analysis – NTQ ; Funding acquisition – KP ; Investigation – NTQ, FR, JE, VC, PL ; Project administration – CA, NTQ ; Supervision –CA, KP ; Validation –CA, NTQ ; Visualization – NTQ, FR ; Writing – original draft – CA, TDP, NTQ, FR ; Writing – review & editing – CA, TDP, KP, NTQ, FR

VI. References

1. D. Çelik and M. Yıldız, *Int. J. Hydrog. Energy*, 2017, **42**, 23395-23401.
2. M. W. Kanan and D. G. Nocera, *Science*, 2008, **321**, 1072.
3. A. M. Müller, *Chem. Rev*, 2016, **116**, 14120−14136.
4. T. F. Jaramillo, *JACS*, 2013, **135**, 16977−16987.
5. N.-T. Suen, S.-F. Hung, Q. Quan, N. Zhang, Y.-J. Xu and H. M. Chen, *Chem. Soc. Rev.*, 2017, **46**, 337-365.
6. R. Kötz, S. Stucki, D. Scherson and D. M. Kolb, *Journal of Electroanalytical Chemistry and Interfacial Electrochemistry*, 1984, **172**, 211-219.
7. F. Song, L. Bai, A. Moysiadou, S. Lee, C. Hu, L. Liardet and X. Hu, *J. Am. Chem. Soc.*, 2018, **140**, 7748-7759.
8. M. Gong, Y. Li, H. Wang, Y. Liang, J. Z. Wu, J. Zhou, J. Wang, T. Regier, F. Wei and H. Dai, *J. Am. Chem. Soc.*, 2013, **135**, 8452-8455.
9. Z. Lu, W. Xu, W. Zhu, Q. Yang, X. Lei, J. Liu, Y. Li, X. Sun and X. Duan, *Chem. Commun.*, 2014, **50**, 6479-6482.
10. L. Lei, D. Huang, C. Zhou, S. Chen, X. Yan, Z. Li and W. Wang, *Coord. Chem. Rev.*, 2020, **408**, 213177.
11. M. S. Burke, L. J. Enman, A. S. Batchellor, S. Zou and S. W. Boettcher, *Chem. Mater.*, 2015, **27**, 7549-7558.
12. F. Dionigi and P. Strasser, *Advanced Energy Materials*, 2016, **6**, 1600621.
13. M. D. Kärkäs and B. Åkermark, *Dalton Trans.*, 2016, **45**, 14421-14461.
14. Y. Yan, J. Lin, J. Cao, S. Guo, X. Zheng, J. Feng and J. Qi, *J. Mater. Chem. A*, 2019, **7**, 24486-24492.
15. I. E. Wachs, *Catal. Today*, 2005, **100**, 79-94.
16. C. Xuan, J. Wang, W. Xia, J. Zhu, Z. Peng, K. Xia, W. Xiao, Huolin L. Xin and D. Wang, *J. Mater. Chem. A*, 2018, **6**, 7062-7069.
17. M. K. Bates, Q. Jia, H. Doan, W. Liang and S. Mukerjee, *ACS Catal.*, 2016, **6**, 155-161.
18. A. J. Esswein, M. J. McMurdo, P. N. Ross, A. T. Bell and T. D. Tilley, *J. Phys. Chem. C*, 2009, **113**, 15068-15072.
19. Y. Qiu, L. Xin and W. Li, *Langmuir*, 2014, **30**, 7893-7901.
20. R. H. Manso, P. Acharya, S. Deng, C. C. Crane, B. Reinhart, S. Lee, X. Tong, D. Nykypanchuk, J. Zhu, Y. Zhu, L. F. Greenlee and J. Chen, *Nanoscale*, 2019, **11**, 8170-8184.
21. J. Qiao, F. Song, J. Hu, D. Huo, J. Yuan, J. Shen, L. Niu and A.-j. Wang, *Int. J. Hydrog. Energy*, 2019, **44**, 16368-16377.
22. V. Gatard, D. De Masi, R. Chattot, I. M. Marin, J. M. A. Revert, P.-F. Fazzini, T. Encinas, V. Martin, S. Faure, J. Deseure, J. Carrey, B. Chaudret and M. Chatenet, *Electrocatalysis*, 2020, **11**, 567-577.
23. C. Amiens, B. Chaudret, D. Ciuculescu-Pradines, V. Collière, K. Fajerwerg, P. Fau, M. Kahn, A. Maisonnat, K. Soulantica and K. Philippot, *New J. Chem.*, 2013, **37**, 3374-3401.
24. C. Amiens, D. Ciuculescu-Pradines and K. Philippot, *Coord. Chem. Rev.*, 2016, **308**, 409-432.
25. J. De Tovar, N. Romero, S. A. Denisov, R. Bofill, C. Gimbert-Suriñach, D. Ciuculescu-Pradines, S. Drouet, A. Llobet, P. Lecante, V. Colliere, Z. Freixa, N. McClenaghan, C. Amiens, J. García-Antón, K. Philippot and X. Sala, *Mater. Today Energy*, 2018, **9**, 506-515.
26. L. Mallón, N. Romero, A. Jiménez, E. Martín Morales, J. Alemán, R. Mas-Ballesté, R. Bofill, K. Philippot, J. García-Antón and X. Sala, *Catal. Sci. Technol.*, 2020, **10**, 4513-4521.
27. Q. T. Nguyen, E. Rousset, V. T. H. Nguyen, V. Colliere, P. Lecante, W. Klysubun, K. Philippot, J. Esvan, M. Respaud, G. Lemercier, P. D. Tran and C. Amiens, *ACS Appl. Mater. Interfaces*, 2021, **13**, 53829-53840.
28. L. Mallón, C. Cerezo-Navarrete, N. Romero, M. Puche, J. García-Antón, R. Bofill, K. Philippot, L. M. Martínez-Prieto and X. Sala, *New J. Chem.*, 2022, **46**, 49-56.

29. O. Margeat, D. Ciuculescu, P. Lecante, M. Respaud, C. Amiens and B. Chaudret, *Small*, 2007, **3**, 451-458.
30. K. Gharbi, F. Salles, P. Mathieu, C. Amiens, V. Collière, Y. Coppel, K. Philippot, L. Fontaine, V. Montembault, L. S. Smiri and D. Ciuculescu-Pradines, *New J. Chem.*, 2017, **41**, 11898-11905.
31. S. J. Parikh and J. Chorover, *Langmuir*, 2006, **22**, 8492-8500.
32. B. Basly, G. Popa, S. Fleutot, B. P. Pichon, A. Garofalo, C. Ghobril, C. Billotey, A. Berniard, P. Bonazza, H. Martinez, D. Felder-Flesch and S. Begin-Colin, *Dalton Trans.*, 2013, **42**, 2146-2157.
33. S. Mohapatra and P. Pramanik, *Colloids Surf., A: Physicochem. Eng. Asp.*, 2009, **339**, 35-42.
34. R. D. Ramsier, P. N. Henriksen and A. N. Gent, *Surf. Sci.*, 1988, **203**, 72-88.
35. T. J. Daou, S. Begin-Colin, J. M. Grenèche, F. Thomas, A. Derory, P. Bernhardt, P. Legaré and G. Pourroy, *Chem. Mater.*, 2007, **19**, 4494-4505.
36. T. Radu, C. Iacovita, D. Benea and R. Turcu, *Appl. Surf. Sci.*, 2017, **405**, 337-343.
37. T. Yamashita and P. Hayes, *Appl. Surf. Sci.*, 2008, **254**, 2441-2449.
38. K. Yang, H. Peng, Y. Wen and N. Li, *Appl. Surf. Sci.*, 2010, **256**, 3093-3097.
39. D. A. Corrigan, *J. Electrochem. Soc.*, 1987, **134**, 377-384.
40. D. A. Corrigan and R. M. Bendert, *J. Electrochem. Soc.*, 1989, **136**, 723-728.
41. M. Wehrens-Dijksma and P. H. L. Notten, *Electrochim. Acta*, 2006, **51**, 3609-3621.
42. L. Trotochaud, J. K. Ranney, K. N. Williams and S. W. Boettcher, *J. Am. Chem. Soc.*, 2012, **134**, 17253-17261.
43. I. C. Man, H.-Y. Su, F. Calle-Vallejo, H. A. Hansen, J. I. Martínez, N. G. Inoglu, J. Kitchin, T. F. Jaramillo, J. K. Nørskov and J. Rossmeisl, *ChemCatChem*, 2011, **3**, 1159-1165.
44. Y.-H. Fang and Z.-P. Liu, *J. Am. Chem. Soc.*, 2010, **132**, 18214-18222.
45. D. A. Marcel Risch, *ChemRxiv*, 2021, DOI: 10.26434/chemrxiv-2021-hgbq6.
46. W. Ma, R. Ma, C. Wang, J. Liang, X. Liu, K. Zhou and T. Sasaki, *Acs Nano*, 2015, **9**, 1977-1984.
47. L. Trotochaud, S. L. Young, J. K. Ranney and S. W. Boettcher, *J. Am. Chem. Soc.*, 2014, **136**, 6744-6753.
48. L. Zaramello, B. L. Albuquerque, J. B. Domingos and K. Philippot, *Dalton Trans.*, 2017, **46**, 5082-5090.
49. L.-M. Lacroix, S. Lachaize, A. Falqui, T. Blon, J. Carrey, M. Respaud, F. Dumestre, C. Amiens, O. Margeat, B. Chaudret, P. Lecante and E. Snoeck, *J. Appl. Phys.*, 2008, **103**, 07D521.

SUPPLEMENTARY INFORMATIONS

for

Synthesis of NiFeOx nanocatalysts from metal-organic precursors for the oxygen evolution reaction

Nguyen Thi Quyen,[1,2,3] Francois Robert, [1,2] Vincent Colliere,[1,2] Pierre Lecante,[4] Karine Philippot,[1,2] Jérome Esvan, [5] Tran Dinh Phong,[3]* Catherine Amiens,[1,2]*

[1] CNRS, LCC (Laboratoire de Chimie de Coordination), 205 Route de Narbonne, BP 44099, F-31077 Toulouse Cedex 4, France.
[2] Université de Toulouse, UPS, INPT, F-31077 Toulouse Cedex 4, France
[3]University of Science and Technology of Hanoi, Vietnam Academy of Science and Technology of Hanoi, 18 Hoang Quoc Viet, Hanoi, Vietnam.
[4]CEMES-CNRS, Université de Toulouse, CNRS, UPS, 29 rue J. Marvig, 31055 Toulouse, France
[5]CIRIMAT, Université de Toulouse, CNRS-INPT-UPS, 4 Allée Emile Monso, BP 44362, 31030 Toulouse, France

1. **Complementary data on the NP characterization.**

a. **Transmission electron microscopy**

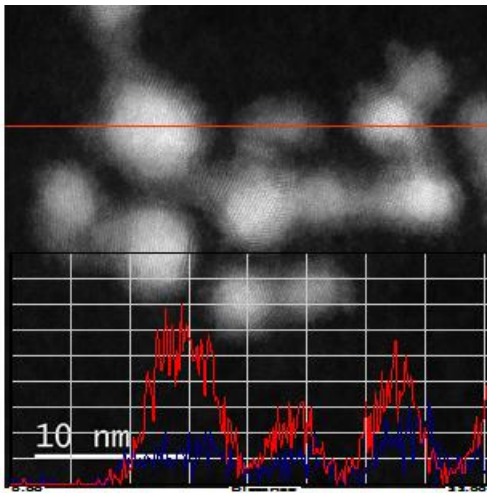

Figure S1. *STEM HAADF (JEM-ARM200F) image of NiFeOx-2/1, and EDX analysis along the horizontal red line: top red and bottom blue curves represent the Fe and Ni contents, respectively.*

a) *b)*

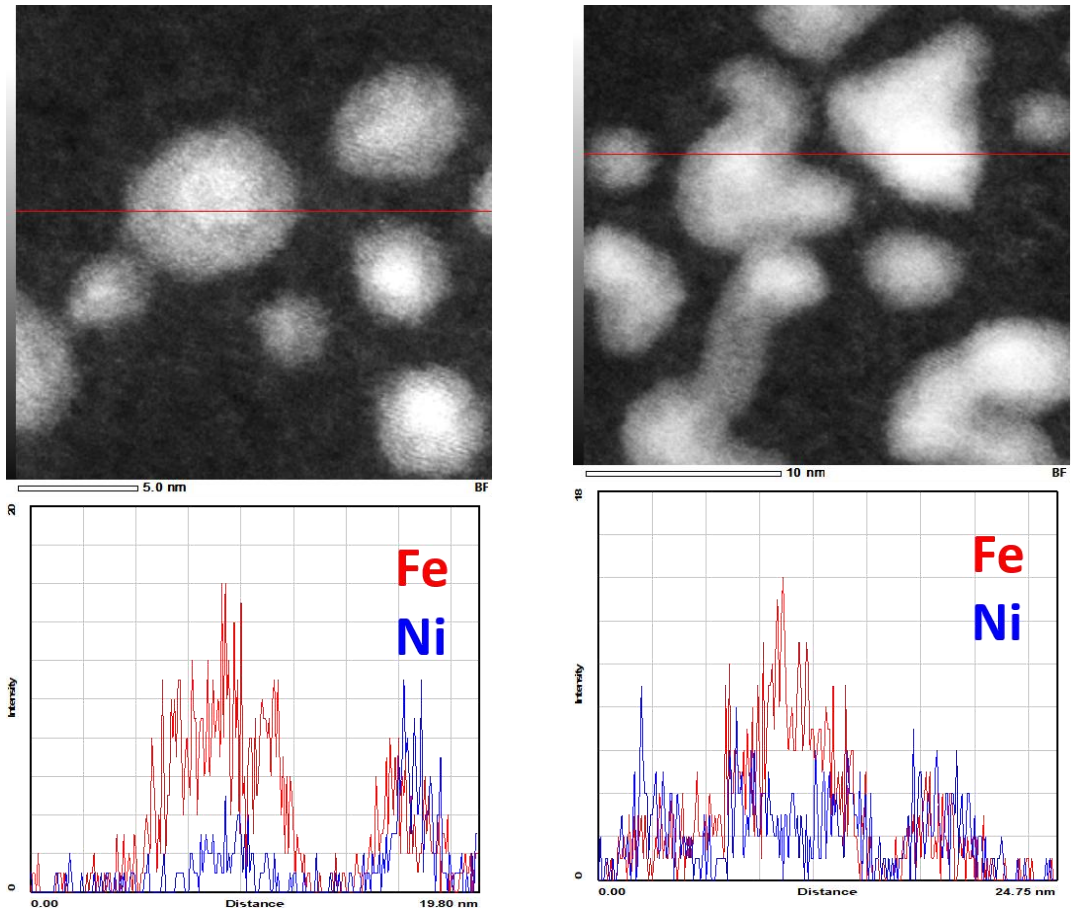

Figure S2. *STEM HAADF (JEMARM200F) images of NiFeOx–1/1 (top) and EDX analysis along the horizontal red line in each image (bottom).*

Figures S1 and **S2** show STEM HAADF images of NiFeOx-2/1 and NiFeOx-1/1 samples (recorded on a JEM ARM200F microscope). Clearly, both Ni and Fe are present in the NPs. Drawing any firm conclusion on the distribution of Ni and Fe inside the NPs is however difficult at such small size, especially as ARM is far from being a statistical method. It can be observed that STEM-EDX analysis of a few NPs from sample NiFeOx–2/1 NPs does not show any clear segregation of the two elements (**Figure S1**). Analysis of sample NiFeOx–1/1 NPs is even less conclusive. Under high resolution imaging conditions, three populations of NPs are evidenced: the smallest spherical NPs, in which no clear segregation of the two elements can be distinguished, the largest spherical NPs which present a surface enriched in Fe (**Figure S2a**), and NPs of irregular shape (**Figure S2b**) showing a shell enriched in Ni. These results must be taken with great care due to lack of statistical data. Indeed the more statistical WAXS investigation shows that most of the NPs comprise a Ni fcc core.

b. Infra-red spectroscopy

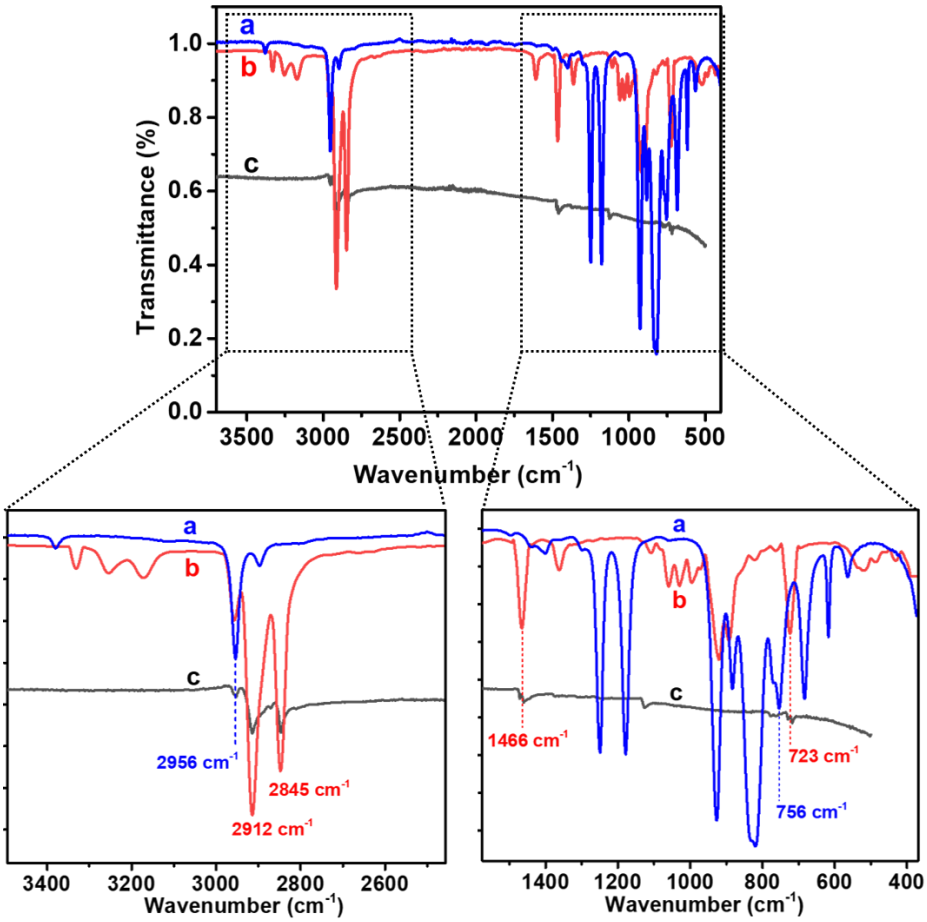

***Figure S3**. FT-IR spectrum of NiFeOx–2/1 (black line, c) compared to reference spectra of HDA (red line, b) and HMDS (blue line, a).*

The two peaks at 2912 cm^{-1} and 2845 cm^{-1} are attributed to vC-H stretching modes of alkyl chains, as in HDA. The peaks at 1466 cm^{-1} and 723 cm^{-1} are attributed to respectively, the CH bending, and CH_2 rocking modes of an alkyl chain, thus confirming the presence of HDA. The absence of peaks in the 1200-800 cm^{-1} region indicates that HMDS, which forms *in situ*[1] is not detected in the powder recovered.

c. Water transfer process

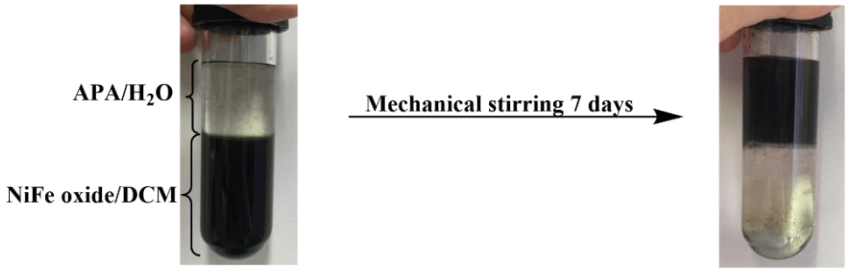

Figure S4. *Pictures of the ligand exchange process.*

2. Synthesis and characterization of the reference samples

Ni and Fe oxide monometallic references were prepared following the synthetic pathways described in **Scheme S1**.

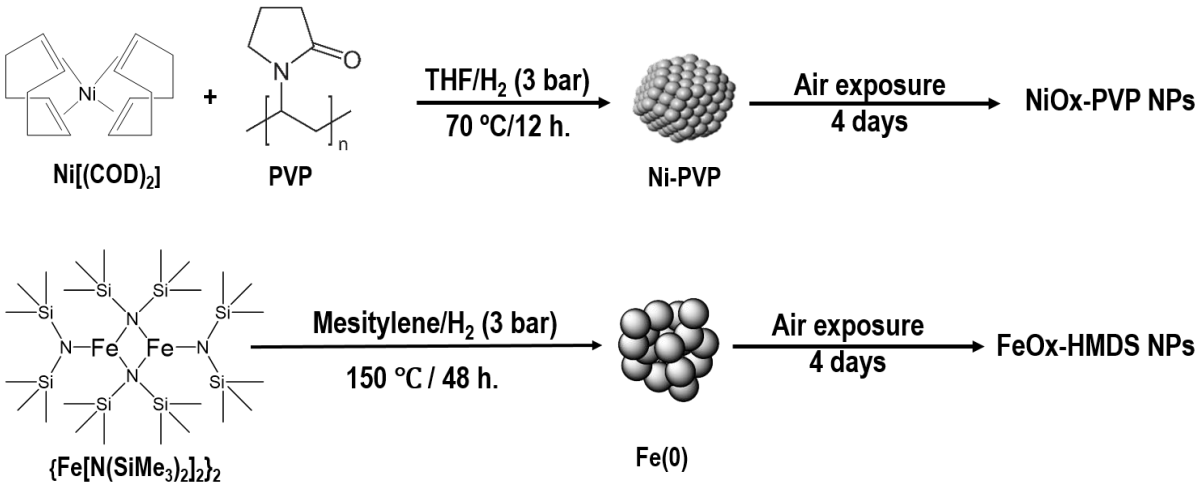

Scheme S1. *Synthesis of Ni (top) and Fe (bottom) oxide reference samples*

Ni[2] and Fe[3] NPs were synthesized following previous publications from our group. Briefly, the Ni NPs were obtained by hydrogenation of the biscyclooctadiene nickel(0) complex (THF, 70 °C, 12 h) in the presence of polyvinylpyrrolidone (PVP) as stabilizer, leading to a nanomaterial with a Ni loading of 9.0 wt% based on ICP-OES data. Fe NPs were synthesized by hydrogenation of the di-bis(bistrimethylsilylamido)iron (II) complex, $[Fe(N(SiMe_3)_2)_2]_2$ (mesitylene, 150 °C, 48 h). The Fe NPs thus obtained are stabilized by HMDS which forms *in situ*. The Fe content determined by ICP-OES is 56 wt%.

As for the NiFe NPs, the as-prepared Ni and Fe NPs were oxidized in air for 4 days, in the solid state. The final nanomaterials are referred to as NiOx-PVP and FeOx-HMDS.

TEM images of NiOx-PVP (**Figure S5a**) revealed the presence of mostly spherical particles with an average size of 3.9 ± 2.1 nm (**Figure S5b**), comparable to that of NiFeOx-2/1-APA and NiFeOx-1/1-APA.

Analysis of the TEM images of FeOx-HMDS indicates that the NPs are also spherical in shape with an average size of 1.6 ± 0.7 nm (**Figure S6**).

a) b)

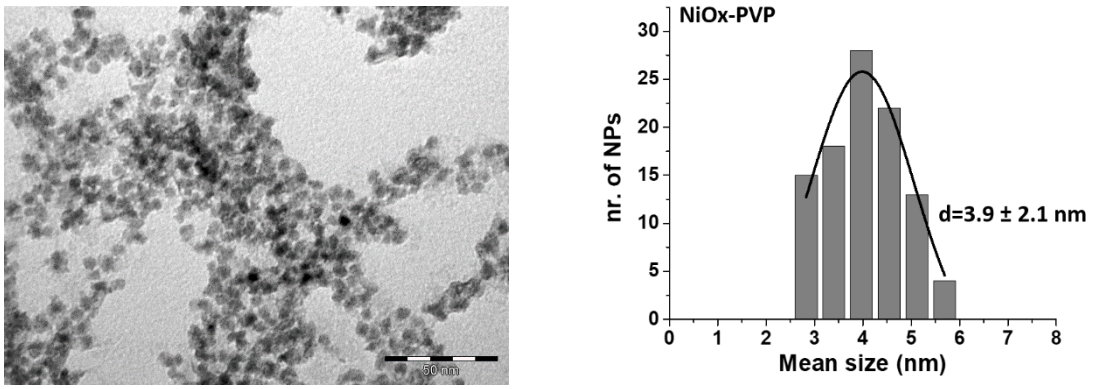

Figure S5*. TEM image of NiOx-PVP (a)(scale bar = 50 nm) and corresponding size histogram (b)*

a)

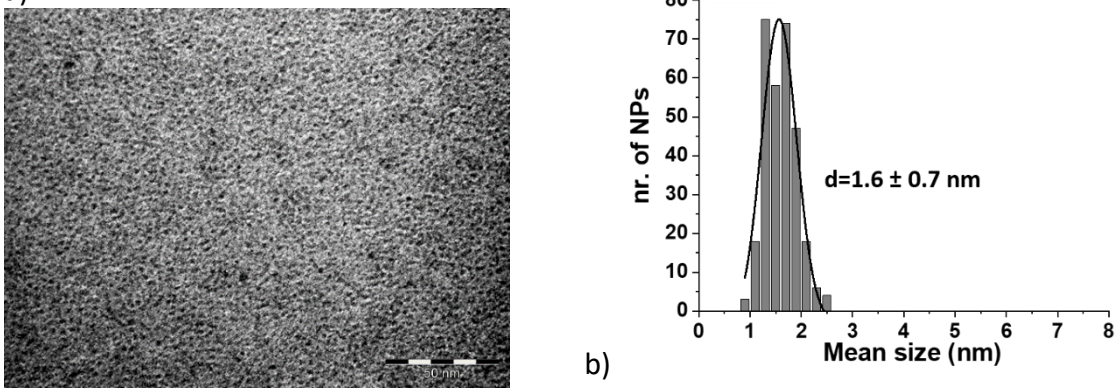

b)

Figure S6*. TEM image of FeOx-HMDS (a)(scale bar = 50 nm) and corresponding size histogram (b).*

a. Structural and electronic characterization of NiOx-PVP :

The sample was analyzed by WAXS to identify the oxide formed (**Figure S7**). Upon oxidation, an increment in the amorphous contribution is noted, but no new diffraction peaks can be observed. Rather, the fcc Ni contribution which is clearly observed in the Ni NPs diagram still dominates the NiOx-PVP diagram. This indicates that oxidation of the Ni NPs in dry conditions produces a passivating amorphous surface layer.

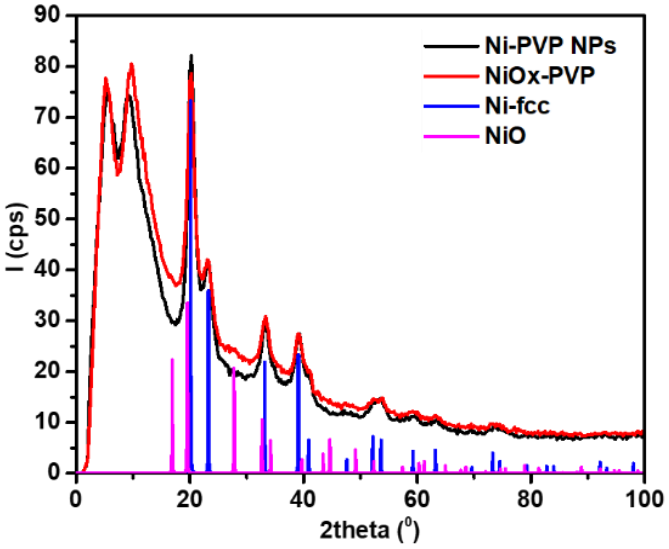

Figure S7. WAXS *diagrams of Ni-PVP reproduced from ref.*[2]*, NiOx-PVP, Ni-fcc (PDF 04-010-6148), and NiO reference pattern (PDF 04-010-6148)*

To identify this amorphous layer, an XPS study was attempted. An aqueous dispersion of the sample was drop casted on a FTO electrode (in conditions used to assess the catalytic activity of the NPs in OER) and studied by XPS. The Ni2p spectrum showed two peaks at 855.9 eV and 861.5 eV which were assigned to Ni^{2+} in a hydroxide environment ($Ni(OH)_2$)(**Figure S8**). No peaks of metallic Ni were found. Given the depth probed by XPS (*circa* 5 nm) and the average size of the NPs (3.9 ± 2.1 nm), this suggests that the passivation afforded by the amorphous surface layer formed upon air oxidation in the solid state was not effective in water. As the NiOx-PVP NPs quickly evolved upon dispersion in water, we thus couldn't identify this first formed amorphous layer. However, this study shows that once deposited on the FTO electrode, the oxidation state of Ni in this sample is comparable to that of Ni at the surface of the NiFeOx-2/1-APA and NiFeOx-1/1-APA nanocatalysts.

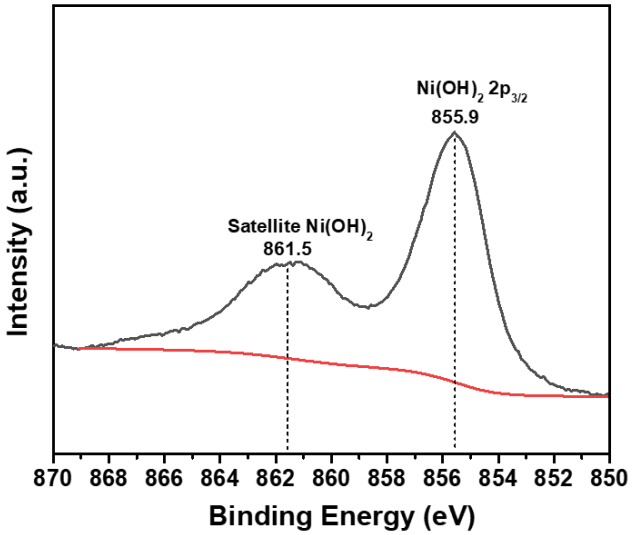

***Figure S8**. Ni 2p XPS spectrum of NiOx-PVP deposited on a FTO substrate.*

b. Structural and electronic characterization of FeOx-HMDS :

WAXS measurements were performed on FeOx-HMDS (**Figure S9**). The Radial Distribution Function calculated from the data displays peaks at 0.19 and 0.32 nm close to the values of the Fe-O and Fe-Fe bonds (in the Fe-O-Fe sequence) that are typical of an oxide. No direct Fe-Fe bonds is observed indicating the full oxidation of the NPs. The size of the crystalline domains is however too small for the structure to be identified unambiguously.

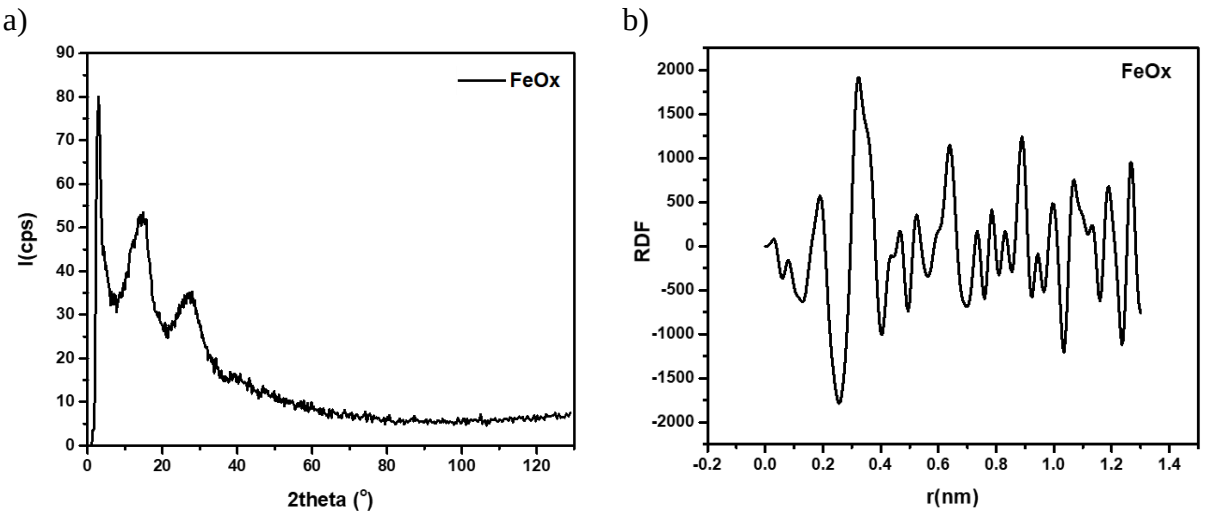

***Figure S9**. a) WAXS diagram and b) RDF of FeOx-HMDS after oxidation in air for 4 days.*

After drop-casting a dispersion of the NPs in a mixture of EtOH/H_2O/Nafion (see experimental part - preparation of catalyst ink) on a FTO support, only one Fe 2p peak can be

observed in the XPS spectrum (**Figure S10**). The binding energy (711.5 eV) corresponds to Fe^{3+} ions like in the oxidized bimetallic NiFeOx-2/1-APA and NiFeOx-1/1-APA nanocatalysts.

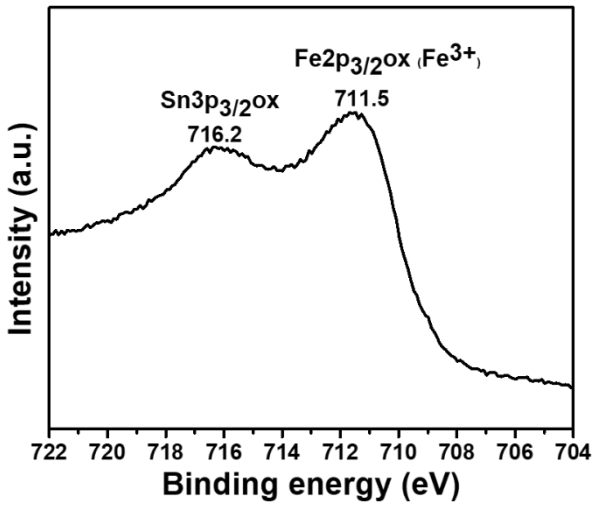

***Figure S10**. Fe 2p XPS spectrum of FeOx-HMDS NPs deposited on FTO.*

3. Details on the synthesis and characterization of NiFeOx-1/9-HMDS

Synthesis of 1Ni/9Fe-HMDS NPs was performed using the adequate ratio of the Ni and Fe precursors, namely 1 $Ni(COD)_2$, 4.5 $[Fe(N(SiMe_3)_2)_2]_2$, and the synthesis pathway used to prepare the reference Fe NPs (**Scheme S1**, bottom). As for the Fe NPs, the final nanomaterial consisted in NPs stabilized by HMDS formed *in situ*.

Once oxidized, the NPs (hereafter referred to as NiFeOx-1/9-HMDS) was characterized by TEM, WAXS and XPS. The TEM image of NiFeOx-1/9-HMDS, **Figure S11a**, shows well dispersed NPs with a mean size of 1.3 ± 0.6 nm (**Figure S11b**) comparable with the average size of the NPs in FeOx.

a) b)

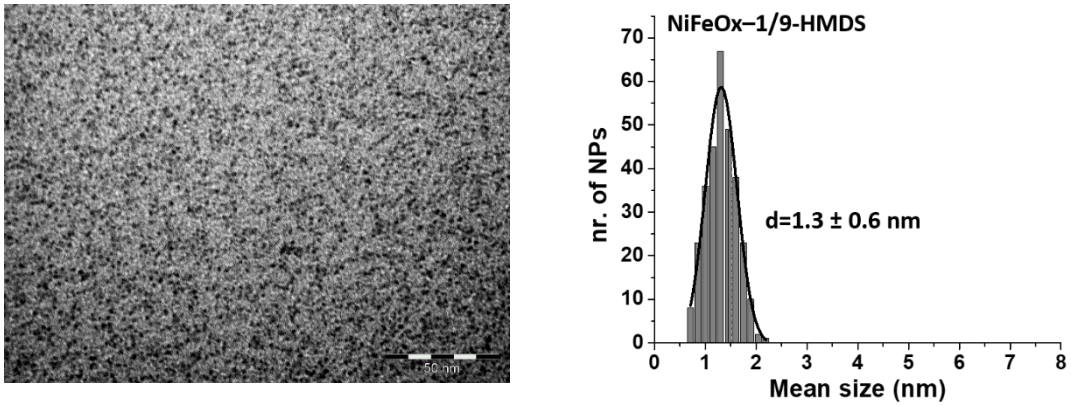

***Figure S11**. TEM image of a) NiFeOx-1/9-HMDS (scale bar = 50 nm)and b) corresponding size histogram d = 1.3 ± 0.6 nm.*

Figure S12 shows the WAXS diagrams and RDFs of NiFeOx-1/9-HMDS and FeOx-HMDS. As can be seen from this figure, the structure of NiFeOx-1/9–HMDS presents only a short range order, as in FeOx-HMDS.

a) b)

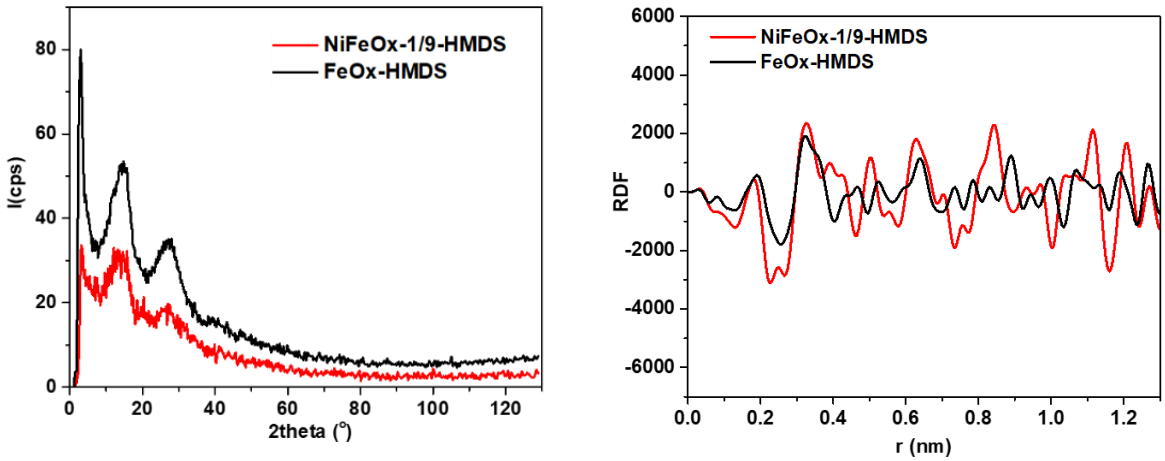

***Figure S12**. a) WAXS diagrams and b) RDFs of NiFeOx-1/9-HMDS and FeOx-HMDS*

After drop-casting of a dispersion of the NPs in a mixture of EtOH/H_2O/Nafion (see experimental part - preparation of catalyst ink) on a FTO support the Fe 2p XPS spectrum of NiFeOx-1/9-HMDS presents one peak located at 711.6 eV characteristic of Fe^{3+}(**Figure S13**). The Ni2p spectrum displays a main peak at 856.1 eV attributed to $Ni(OH)_2$. The presence of Ni metal in the sample is ambiguous due to the poor signal/noise ratio in the 852 – 853 eV region (**Figure S14**). The electronic state of Fe and Ni in these NPs is thus similar to the one in the bimetallic NiFeOx-2/1-APA and NiFeOx-1/1-APA nanocatalysts.

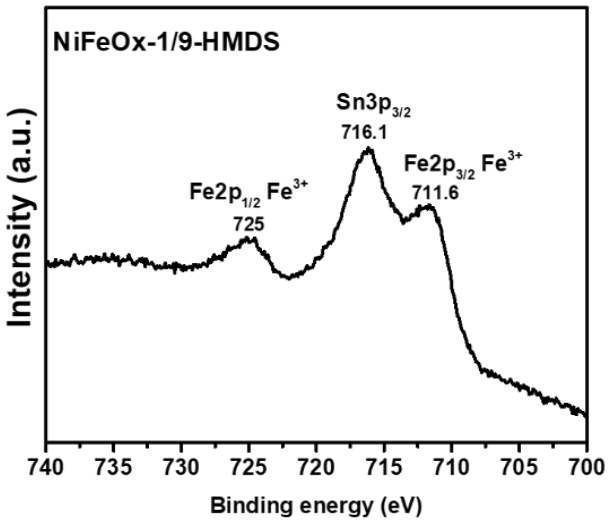

***Figure S13**. Fe 2p XPS spectrum of NiFeOx-1/9-HMDS deposited on FTO*

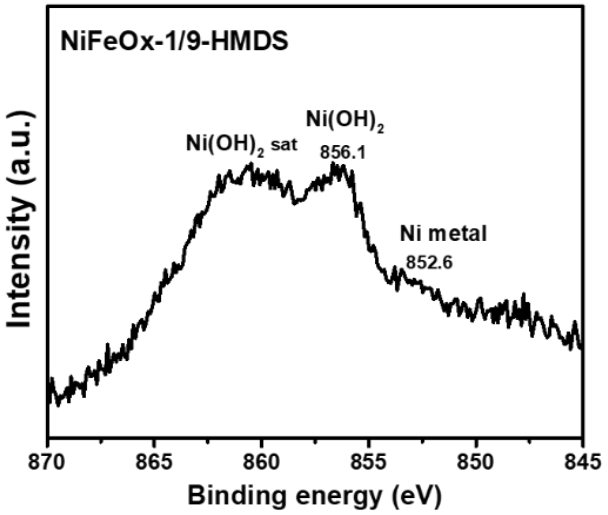

***Figure S14**. Ni 2p XPS spectrum of NiFeOx-1/9-HMDS deposited on FTO*

The Fe and Ni contents were 27 wt% and 3 wt%, respectively, based on ICP analysis. We consider that these NPs consist in an amorphous NiFe oxide of 1Ni9Fe composition bearing only HMDS ligands at their surface.

4. Calculation of TOF values:

The molar amounts of metal atoms (Ni and Fe) in the NiFeOx-2/1-APA and NiFeOx-1/1-APA NPs were determined by ICP-OES analysis, from which the quantity of each element deposited on the electrode could be calculated.

***Table 1**. Details on calculating TOF values for sample NiFeOx-2/1-APA, NiFeOx-1/1-APA, and NiFeOx-1/9-HMDS*

	NiFeOx-2/1-APA	NiFeOx-1/1-APA	NiFeOx-1/9-HMDS
ICP %Ni	63	44	3
ICP %Fe	29	42	27
Concentration of catalyst ink (mg/ml)	3	3	3
Volume deposited (µl)	17	17	17
Mass deposited (mg)	0.051	0.051	0.051
Mol of Fe deposited (mol)	2.64107E-07	3.825E-07	2.45893E-07
Mol of Ni deposited (mol)	5.44576E-07	3.80339E-07	2.59322E-08
Mol of metal atoms deposited (mol)	8.08683E-07	7.62839E-07	2.71825E-07
j at η = 400 mV (mA/cm^2)	26.17	18.27	3.65
I at η = 400 mV (mA)	5.12932	3.58092	0.7154
Mol of O_2 produced (mol)	1.32905E-08	9.27844E-09	1.85366E-09
TOF (s^{-1})	**0.016**	**0.012**	**0.007**

The number of moles of O_2 produced per second was calculated from the current density measured at an overpotential of 400mV, knowing the geometric area of the electrode (0.196 cm^2) and considering that removal of 4 moles of e^- is necessary to produce 1 mole of O_2 (Faraday constant: 96500 C.mol^{-1}; molar mass of Ni taken as 59 g.mol^{-1}, and molar mass of Fe taken as 56 g.mol^{-1}). The turnover number (TOF) was calculated by dividing the number of moles of O_2 produced per second by the total number of moles of metal atoms (following the method of Qiu *et al.*[4]).

5. References

1. O. Margeat, D. Ciuculescu, P. Lecante, M. Respaud, C. Amiens and B. Chaudret, *Small*, 2007, **3**, 451-458.
2. L. Zaramello, B. L. Albuquerque, J. B. Domingos and K. Philippot, *Dalton Trans.*, 2017, **46**, 5082-5090.
3. L.-M. Lacroix, S. Lachaize, A. Falqui, T. Blon, J. Carrey, M. Respaud, F. Dumestre, C. Amiens, O. Margeat, B. Chaudret, P. Lecante and E. Snoeck, *J. Appl. Phys.*, 2008, **103**, 07D521.
4. Y. Qiu, L. Xin and W. Li, *Langmuir*, 2014, **30**, 7893-7901.

6. Abbreviations

APA	3-aminopropyl phosphonic acid
ARM	Atom resolved microscopy
ATR	Attenuated total reflectance
CNTs	Carbon nanotubes
COD	biscyclooctadiene
CVs	Cyclic voltammetrys
DCM	Dichloromethane
EtOH	Ethanol
EDX	Energy dispersive X-ray spectroscopy
FTO	Fluorine-doped tin oxide
FT-IR	Fourier transform infrared
HAADF-STEM	High angle annular dark field-scanning transmission electron microscopy
HDA	Hexadecylamine
HER	Hydrogen evolution reaction
HMDS	Hexamethyldisilazane
HR-TEM	High resolution-transmission electron microscopy
ICP-OES	Inductively coupled plasma-optical emission spectroscopy
LSV	Linear sweep voltammetry
NPs	Nanoparticles
OER	Oxygen evolution reaction
RHE	Reversible hydrogen electrode
SCE	Saturated Calomel Electrode
TEM	Transmission electron microscopy
THF	Tetrahydrofuran
TOF	Turn over frequency
WAXS	Wide angle X-ray scattering
WOCs	Water oxidation catalysts
WS	Water splitting
XPS	X-ray photoelectron spectroscopy